Compliance Model-based Contact Force Control for Soft Continuum Robots

Jialei Shi*†, Sara-Adela Abad†‡, Jian S Dai§¶, and Helge Wurdemann†

Abstract

Soft robots are increasingly being explored and developed in various settings that demand safe and adaptable interactions between robots and their environments. In addition, soft robots exhibit passive compliant behaviour and generate continuous deformations when engaging with the environments. This imposes challenges on achieving active, on-demand interaction force control, especially when feedback force sensing devices are not available. Consequently, there is a need to explore new model-based force control paradigms for soft robots. In this paper, we propose a (quasi-)static force control approach for soft robots based on the compliance modelling, avoiding the necessity for feedback control loops or extensive training data collection. The proposed approach can deliver contact force control along three Cartesian axes when the robot is actuated into various configurations. The compliance matrix is derived with the robot configuration, which allows the calculation of desired deflection displacements needed to generate on-demand forces. The resulting force control is achieved by solving inverse kinematics problems based on these deflection displacements. The efficacy of our proposed controller is validated through experiments with both one- and two-segment pneumatic-driven soft continuum robots. The results demonstrate effective static force control performance, with mean control errors below 5% of the desired peak forces.

Keywords: Soft Continuum Robots, Pneumatic Actuators, Force Control, Compliance Model

Introduction

Soft robots, made of compliant materials, offer inherent safety when interacting with their environment.[1,2] For traditional rigid-link robots, interaction forces in the task space are provided and regulated by controlling torque or displacement in the joint space, often using impedance or admittance control strategies.[3] In contrast, soft robots generate interaction forces through self-deformation. The deformability of soft robots mitigates contact uncertainties and results in more adaptive robot-environment interactions, which is especially valuable for innovations in collaborative robots[4] and next-generation medical robots.[5,6] However, the inherent robot compliance that makes soft robots advantageous also poses challenges for actively controlling and applying precise forces in desired directions.[7]

To regulate the Cartesian forces of soft continuum robots, force control techniques traditionally used in rigid-link robots can be adopted. A prominent force control approach is discretising soft robots into finite elements and regulating virtual joint forces from each element using Jacobian projection.[8] For instance, an intrinsic force sensing approach was proposed to estimate the wrench exerted at a tendon-driven continuum robot tip by monitoring the actuation forces.[9] Consequently, this estimated wrench is further advanced as feedback information to implement closed-loop

*Hamlyn Centre for Robotic Surgery, Department of Mechanical Engineering, Imperial College London, UK.
†Department of Mechanical Engineering, University College London, UK.
‡Universidad Nacional de Loja, Loja, Ecuador.
§Institute for Robotics, Southern University of Science and Technology, Shenzhen, China.
¶Centre for Robotics Research, Department of Engineering, King's College London, UK.

force control.[10] Specifically, a hybrid motion and force control approach was proposed for tendon-driven continuum robots, achieving force regulation or contact surface estimation from sensed forces in the task space. In these cases, actuation forces are typically obtained from force transducers in tendon-driven or parallel continuum robots.[11,12] However, for fluidic-driven robots, additional considerations are required to convert fluidic pressure or volume into generalised actuation forces or torques.[13] An inverse dynamics controller was proposed to regulate the in-plane Cartesian impedance for pneumatic-driven soft robots interacting with their environment, based on the assumption of piecewise constant curvature.[14] For hydraulic-driven soft robots, a combination of fluid volume and pressure can be used for intrinsic force sensing and control in soft parallel robotic systems.[15]

In addition to model-based force sensing and control, technological advances have enabled the integration of force sensing devices into soft robots. For instance, forces exerted on the robot can be measured directly using attached force/torque (F/T) sensors.[16] However, since F/T sensors are typically rigid, their embedding in soft robots presents challenges. In contrast, fibre optics, which are inherently flexible,[17] can measure forces by detecting strains. For example, stretchable sensors based on optical waveguides have been developed for applications such as prosthetic hands.[18] Additionally, advances in materials science have led to the development of flexible force sensors using technologies like piezoelectric polymers,[19] liquid metals,[20,21] and pneumatic fluids.[22] Moreover, fusion of sensed information and models offers new perspectives on interaction force estimation and regulation of soft robots.[23,24] A vision-based external forces sensing approach was proposed in combination with finite element method, where the intensities and the locations of the external forces can be estimated.[25] Similarly, the deformation of soft robots derived from motion tracking can be utilised to achieve force and motion control,[26] as well as estimate and attenuate external force disturbances.[27,28]

Another force sensing and control paradigm for soft robots is the data-driven approach.[29–31] One such method is a sensorless force and displacement estimation technique that relied solely on fluidic pressure and volume in a pneumatically driven soft actuator.[32] Additionally, a learning-based closed-loop force control strategy was developed by integrating embedded soft sensors with recurrent neural networks, allowing the system to effectively handle significant drift and hysteresis in feedback signals.[33] It is important to note that the performance of data-driven approaches depends heavily on the quality and diversity of the training data, which can also limit their generalization and efficacy.

Achieving on-demand force control in specific directions poses significant challenges,[34] particularly in applications where size constraints or the inherent softness of the robot[35] hinder the integration of force sensors, such as in minimally invasive surgery.[36] In these cases, developing force control strategies that do not rely on force sensing devices or large datasets for training could greatly expand the applicability of soft robots.

[Table 1 about here.]

As highlighted in Table 1, this work advances the model-based, (quasi-)static force control techniques for pneumatic-driven soft continuum robots. Specifically, our approach builds on a compliance model. To achieve the force control, we can obtain the compliance matrix under a certain robot configuration determined using the Cosserat rod model. Using this compliance matrix and the desired force, we calculate the target deflection, which in turn defines the new robot configuration. The actuation pressure required to achieve this configuration is then obtained by solving the inverse kinematics of the Cosserat rod model, which we implement using a shooting method. The effectiveness of the proposed method is experimentally validated using one- and two-segment soft robots, demonstrating satisfactory force control accuracy. For example, mean force errors are below 5% of the desired peak forces.

In summary, the key contributions of this work are: 1). The development and validation of a novel on-demand Cartesian force control method for soft continuum robots (see Figure 1(a)) that solely relies on the robot's compliance model, without the need for integrated feedback loops such as

force estimation or sensing. 2). Various multi-axis force control strategies are realised. For instance, robots' tip forces along the x-, y and z-axes can be controlled under different robot configurations. Notably, when implementing the force controller on a two-segment robot, both uniform force control and distal-only force control can be achieved (see Figure 1(b)).

[Figure 1 about here.]

Materials and Method

Soft robotic prototype

The main body of the soft robot is made of a highly deformable elastomer (Ecoflex 00-50, SmoothOn) with a pneumatic-driven principle.[16,37] To seal the actuation chambers at both ends, a stiffer material, Dragon Skin 30, is used. The robot has six individually reinforced circular chambers. Since two adjacent chambers are connected as one pair, $\mathcal{P}_i$ is used to denote the pressure in the ith chamber pairs. As illustrated in Figure 1(a), $i \in [1,3]$ and $i \in [4,6]$ denote the pressure in the proximal (close to the fixed base) and distal segments, respectively. As such, for a one-segment robot, the pressure vector $P = [\mathcal{P}_1, \mathcal{P}_1, \mathcal{P}_2, \mathcal{P}_2, \mathcal{P}_3, \mathcal{P}_3]$; for a two-segment robot, the pressure vector $P = [\mathcal{P}_1, \mathcal{P}_1, \mathcal{P}_2, \mathcal{P}_2, \mathcal{P}_3, \mathcal{P}_3, \mathcal{P}_4, \mathcal{P}_4, \mathcal{P}_5, \mathcal{P}_5, \mathcal{P}_6, \mathcal{P}_6]$.

Architecture of the compliance model-based force control

The compliance model-based force control architecture is in Figure 1(a). A compliance model is used to compute both the robot's compliance and its configuration under an initial actuation pressure. Once the compliance matrix C^o at a given robot configuration g_c is obtained, the target deflection can be used to get the new robot configuration, named deformed configuration g_d, using this compliance matrix and the desired force f_d. The actuation pressure required to achieve this configuration, and thereby generate the desired force, is then determined by solving the inverse kinematics. Accordingly, the following sections elaborate on the compliance model, derivation of robot deflection and the formulation of the force control problem as inverse kinematics problems.

Configuration-dependent compliance modelling

The compliance behaviour of continuum robots varies under different robot configurations.[12,34,38] In this work, the configuration-dependent compliance of the robot is computed with its configuration, which is modelled using the Cosserat rod model. This integrated approach enables efficient computation of the compliance matrix at any arbitrary point along the robot's body and across different configurations, without increasing the complexity of solving the ordinary differential equations (ODEs) in the Cosserat rod model. The connection between the compliance model and the Cosserat rod model lies in the adjoint matrix Ad_{ob} in (1). Specifically, the configuration-dependent compliance can be described by a set of ODEs with respect to the curve s[39] along the robot's backbone, which yields

$$\begin{cases} p_s(s) = R(s)v(s), \\ R_s(s) = R(s)\hat{u}(s), \\ n_s(s) = -f_e(s) + f_P(s), \\ m_s(s) = -\hat{p}_s(s)n(s) - l_e(s) + l_P(s), \\ C(s)^o_s = \mathrm{Ad}^{-T}_{ob}(s)c^b\mathrm{Ad}^{-1}_{ob}(s), \end{cases} \tag{1}$$

where $s \in [0, L]$ and L is the robot's length. $\hat{(\cdot)}$ is the mapping from $\mathbb{R}^3$ to $\mathfrak{so}(3)$. $p_s(s)$, $R_s(s)$, $n_s(s)$, and $m_s(s)$ are the derivatives of the position vector $p(s)$, the rotation matrix $R(s)$, the internal force $n(s)$, and the internal moment $m(s)$, respectively. $v(s)$ and $u(s)$ are the local strain and the curvature vectors. $f_e(s)$ and $l_e(s)$ are the distributed external force and moment. $c^b = \mathrm{diag}[c^b_{se}, c^b_{bt}]$, is compliance density matrix in the body frame. $c^b_{se} = \mathrm{diag}[GA, GA, EA]^{-1}$, $c^b_{bt} = \mathrm{diag}[EI_x, EI_y, GJ_z]^{-1}$. G and E and are the shear and Young's moduli. I_x, I_y and J_z are the second moment of area around the x, y and z- axes. Ad_{ob} is the adjoint matrix.[39] $f_P(s)$ and $l_P(s)$ are the distributed force and moment from pressurisation, with analytical forms reported in Supplementary Appendix SA1. Equation (1) describes both the robot configuration ($p(s)$, $R(s)$) and the general 6×6 compliance matrix $C(s)^o$ written in the global frame. Moreover, to accommodate for a nonlinear strain-stress relation, a pressure-dependent dynamic modulus $E = h(P)$ can be introduced,[40] where $h(P)$ is a nonlinear function (see Equation (10)).

To solve Equation (1), boundary value problems can be formulated considering force and moment balances at robot's tip. Shooting methods can then be employed to derive solutions via numerical optimisation.[39,41] To obtain the configuration-dependent compliance of soft robot, the objective function is defined as

$$\begin{aligned} \min_{g(0)} \ & ||e_n||^2 + ||e_m||^2, \quad g(0) = [n_0, m_0]. \\ \text{s.t.} \ & e_n = n(t^-) - F_P(t^-) - F_e(t^+), \\ & e_m = m(t^-) - m_P(t^-) - m_e(t^+), \\ & b_c = 0 \text{ (for a two-segment robot)}, \end{aligned} \tag{2}$$

where $g(0)$ is the initial guessing values and includes the unknown force n_0 and moment m_0 at the manipulator's base. The superscripts $^-$ and $^+$ denote the left and right limits. $F_e(t^+)$ and $m_e(t^+)$ are the external applied tip force and moment. $F_P(t^-)$ and $m_P(t^-)$ are the total pressurisation force and moment at the manipulator's tip in the global frame. b_c includes intermediate boundary conditions. Analytical forms of $F_P(t^-)$, $m_P(t^-)$, and b_c are summarised in Supplementary Appendix SA1. The fourth-order Runge–Kutta scheme is adopted for integrating (1).

In summary, the input to the compliance model is the actuation pressure P, and the outputs are the compliance matrix $C(s)^o$, the position vector $p(s)$, and the rotation matrix $R(s)$. The compliance matrix is used to calculated desired deflection subject to the desired force, detailed in the following section.

Robot deflection derivation from desired force

The global tip compliance matrix can be transformed to the body frame via

$$C^b(L) = \mathrm{Ad}_{ob}^T C^o(L) \mathrm{Ad}_{ob}, \tag{3}$$

where C^b is the compliance matrix expressed in the body frame. Considering a desired tip force f_d^o expressed in the global frame, the resulting wrench $\mathbf{W}^b$ expressed in the body frame is

$$\mathbf{W}^b = \begin{bmatrix} R^T & 0_{3\times3} \\ 0_{3\times3} & R^T \end{bmatrix} \begin{bmatrix} f_d^o \\ 0_{3\times1} \end{bmatrix}. \tag{4}$$

As a result, the desired deformed configuration of the robot, i.e., the homogeneous transfer matrix g_d, can be obtained using exponential map, which yields

$$g_d = g_c e^{(\mathbf{b}^b)^\wedge} = g_c e^{(C^b \mathbf{T}^b)^\wedge}, \tag{5}$$

where $\mathbf{T}^b$ is the resulting twist in the body frame. $(\mathbf{T}^b)^\wedge \in \mathbb{R}^{4\times4}$, which writes the twist in the form of an isomorphism matrix in Lie algebra.[39] The deformed tip position vector p_d can be extracted from g_d.

Force control formulated as inverse kinematics problems

Solving (1) - (2) produces robot configurations and the compliance matrix based on actuation pressure. Equation (5) then calculates the deformed tip position p_d using the desired force vector f_d^o. By solving the inverse kinematics problem from p_d, the desired actuation pressure can be obtained to achieve the desired force. In particular, various force control modes can be achieved by formulating different objective functions. For the inverse kinematics, the initial guessing values are

$$g(0) = [n_0, m_0, \mathcal{P}], \tag{6}$$

where $\mathcal{P}$ is the desired pressure vector. $\mathcal{P} \in \mathbb{R}^3$ and $\mathcal{P} \in \mathbb{R}^6$ for one- and two-segment robots, respectively. As illustrated in Figure 1(b), various force control modes can be achieved and are formulated as follows.

For multi-segment soft robots, actuating different segments can produce various force control modes, which is beneficial to vary grasping performances.[42] As such, this work demonstrates two force control modes for a two-segment robot, including uniform force control and distal-only force control modes.

Force control for a one-segment robot: The objective function yields

$$\begin{aligned} \min_{g(0)} \ & ||e_n||^2 + ||e_m||^2 + ||e_t||^2. \\ \text{s.t.} \ & e_n = n(t^-) - F_P(t^-) - F_e(t^+), \\ & e_m = m(t^-) - m_P(t^-) - m_e(t^+), \\ & e_t = p_d - p(t), \ t = L_1. \end{aligned} \tag{7}$$

The desired position p_d is derived from the deformed robot configuration in (5).

Uniform force control for a two-segment robot by coupled pressure: For the uniform force control mode, the pressure from two robot segments is controlled by coupled pressure, i.e., $\mathcal{P}_1 = \mathcal{P}_4$, $\mathcal{P}_2 = \mathcal{P}_5$ and $\mathcal{P}_3 = \mathcal{P}_6$. The objective function is

$$\begin{aligned} \min_{g(0)} \ & ||e_n||^2 + ||e_m||^2 + ||e_t||^2. \\ \text{s.t.} \ & e_n = n(L^-) - F_P(L^-) - F_e(L^+), \\ & e_m = m(L^-) - m_P(L^-) - m_e(L^+), \\ & e_t = p_d - p(t), t = L_1 + L_k + L_2, \\ & b_c = 0, \ \ \mathcal{P}_1 = \mathcal{P}_4, \mathcal{P}_2 = \mathcal{P}_5, \mathcal{P}_3 = \mathcal{P}_6. \end{aligned} \tag{8}$$

Distal-only force control for a two-segment robot by decoupled pressure: In this force control mode, the pressure from two robot segments are controlled independently, meanwhile, the tip force is only generated by the second robot segment.

$$\begin{aligned} \min_{g(0)} \ & ||e_n||^2 + ||e_m||^2 + ||e_t||^2 + ||e_k||^2. \\ \text{s.t.} \ & e_n = n(L^-) - F_P(L^-) - F_e(L^+), \\ & e_m = m(L^-) - m_P(L^-) - m_e(L^+), \\ & e_t = p_d - p(t), t = L_1 + L_k + L_2, \\ & e_k = \Delta p(L_1), \ b_c = 0, \end{aligned} \tag{9}$$

where $\Delta p(L_1)$ denotes that the variation between the desired midpoint position and calculated midpoint position from the forward kinematics of a two-segment robot. In the inverse control, the nonlinear least-square problems from (2) and (7)-(9) are solved using the trust-region approach. The termination tolerance of the summed squared residual errors is set as 10^{-6}.[40]

Experiment hardware

The chamber pressure of the robots is regulated by proportional pressure regulators (Camozzi K8P). A compressor (HYUNDAI HY5508) pressurises air. These pressure regulators are controlled by two Adafruit MCP4728 boards, which receive the command pressure from an Arduino Due via I2C bus. The Arduino board also monitors the chamber pressure and communicates with a host computer (Intel i7, RAM 16 GB) via a serial link. The tip force is measured by an IIT-FT17 6-DoF Force/Torque (F/T) sensor. The host computer runs MATLAB to implement the force control algorithm and processes the experimental data. Detailed descriptions of the experiment hardware are included in our previous work.[43]

Results

Parameter identification

Silicone materials exhibit nonlinear, hyperelastic stress-strain behaviour, influenced by various factors such as strain magnitude, temperature, and humidity.[44] This nonlinearity can be captured by an experimentally identified pressure-dependent dynamic modulus.[40] To achieve this, the elongation-actuation pressure data was required. Figure 2(a) reports the identified parameters of the robots. The elongation displacements of two segments was measured by an NDI tracker attached at the tip of the robot. Based on the averaged elongation-pressure curve (see Figure 2(b)), a second-order polynomial function $h(P)$ is adopted to construct the varying modulus $E(P)$, which yields

$$E(P) = \beta_1 \bar{P}^2 + \beta_2 \bar{P} + \beta_3 = h(P), \tag{10}$$

where $\bar{P}$ is the averaged pressure from three chamber pairs. β_1, β_2 and β_3 are the coefficients of the dynamic modulus. The dynamic modulus $E(P)$ is reported in Figure 2(c), which illustrates that the dynamic modulus monotonically decreases with the pressure.

[Figure 2 about here.]

Blocked force control for a one-segment robot

This experiment validates the tip blocked force control when only one chamber pair (i.e., $\mathcal{P}_1$ is actuated. We examined eight types of time-varying desired forces, which included step force control with an increment of 0.1 N, ramp force control, and sinusoid force control with a force period T of 10 s, 8 s, 6 s, 4 s, 2 s, and 1 s. Throughout all the tests, maximum force magnitude was set as 1.0 N, and the duration of each test was 22 s. The tip force was measured using the F/T sensor (see Figure 3(a)).

Figures 3(b)-(i) depict the force control results. The desired and real forces are represented

in dotted black and red lines, respectively. Figure 3(b) illustrates the controller can achieve satisfying step force control when the desired force increases with an increment of 0.1 N. The controlled force exhibits an overshot force of less than 0.05 N, and the settling time ranges between $0.4 \sim 0.5$ s. Figure 3(c) illustrates that the controller has a stable linearity when tracking a ramp force with a magnitude of 1.0 N. Figures 3(d)-(i) report the results for periodical sinusoid force tracking when the force period varies from 1 s to 10 s. The findings indicate a strong agreement between the desired forces and the actual forces when the force period is within the range of $4 \sim 10$ s. In contrast, Figures 3(h)-(i) illustrate larger deviations between the magnitudes of the desired and real forces. For instance, Figure 3(i) indicates that the real force magnitudes are approximately $0.1 \sim 0.2$ N lower and have a time delay of $0.2 \sim 0.3$ s, compared to the desired forces. Additionally, Supplementary Video S1 reports this experiment.

[Figure 3 about here.]

Figure 4(a) summarises force errors from Figure 3 using boxplots. In the case of step and ramp force tracking, the maximum force errors remain below 0.05 N, while the median errors are around 0.01 N. Compared to the maximum desired force of 1 N, the maximum and median force control errors are 5% and 1%, respectively. For the sinusoid force control, the controller demonstrates consistent accuracy when force periods are of 10 s, 8 s, and 6 s, and maximum and median errors are below 0.16 N and 0.05 N, respectively. As the force period decreases from 4 s to 1 s, force control errors increase. Specifically, the median errors are 0.08 N, 0.12 N, and 0.24 N for force periods of 4 s, 2 s, and 1 s, respectively. Notably, when the force period is 1 s, the maximum error reaches 0.72 N. This suggests that the controller exhibits a cutoff frequency of approximately 0.5 to 1 Hz.

Figure 4(b) demonstrates a strong linear relation between the control pressure and the generated tip blocked force. For example, by a linear regression, the linear coefficients are 1.0 N/bar, 0.92 N/bar and 0.91 N/bar for the ramp force, sinusoid force (T = 10 s) and sinusoid force (T = 4 s) tests, respectively. The shaded colours in Figure 4(b) represent the 95% confidence interval, indicating the level of certainty when fitting a linear relationship.

[Figure 4 about here.]

Force control along three axes for a one-segment robot

This experiment validates the tip force control along the x-, y- and z- axes under different robot configurations. Figure 5(a) illustrates the experimental setup to measure tip forces along three axes. The setup has two linear and two rotational degree of freedoms to position force sensor, allowing the force sensor to be positioned so that the measured forces align with the sensor's z-axis. To achieve the force control along different axes, Figure 5(b) outlines a three-stage processes during the experiments. In the first stage, the robot was first actuated to one of the four configurations: 1) $\mathcal{P}_1 = 1.0$ bar, 2) $\mathcal{P}_3 = 1.0$ bar, 3) $\mathcal{P}_1 = \mathcal{P}_3 = 1.0$ bar and 4) $\mathcal{P}_1 = \mathcal{P}_2 = 1.0$ bar. In the second stage, the robot stabilises for a second. In the third stage, a desired constant force with a specific direction is sent to the controller, which calculates the desired command pressure. As reported in Figure 5(b), the variation of the chamber pressure between the second and third stages generates the desired forces. In the experiments, the desired forces along the x- and y-axes are up to 0.5 N with an increment of 0.1 N. The desired forces along the z-axis are up to 1 N with an increment of 0.2 N.

[Figure 5 about here.]

Figures 6(a)-(d) report the force control results under four configurations. The results show the forces are effectively controlled along three axes, aligning with the desired forces. In general, the real forces settle down after 2 seconds. The mean values and standard deviations of steady-state force errors are reported in Table 2. The results show the mean force errors along the x- and y-axes are less than 0.03 N, with maximum errors smaller than 0.06 N. In the x- and y-axes, the force controller tends to exhibit a better accuracy with the increase of the desired force magnitudes. For example, the mean errors are less than 0.02 N when the desired force is 0.5 N. In contrast, the mean errors can be up to $0.04 \sim 0.06$ N

when the desired force is 0.1 N. In addition, Table 2 shows that the force errors along the z-axis are similar, with the maximum mean errors up to 0.06 N. The standard deviations of the error from Table 2 are about $0.01 \sim 0.02$ N in most cases. In summary, compared to the maximum desired forces, the mean errors are about 6% along the x- and y- axes, and these values are about 5% along the z-axis. The standard deviations of errors are about $2\% \sim 4\%$ of the maximum desired forces. The video demonstration for this experiment is reported in Supplementary Video S2.

[Figure 6 about here.]

[Table 2 about here.]

Uniform force control for a two-segment robot by coupled pressure

This experiment validates the tip force control for a two-segment robot by coupled pressure (i.e., $\mathcal{P}_1 = \mathcal{P}_4$, $\mathcal{P}_2 = \mathcal{P}_5$ and $\mathcal{P}_3 = \mathcal{P}_6$). In this experiment, the two-segment robot was attached to the end-effector of a Franka Emika Panda robotic arm to facilitate the force measurement (see Figure 7). Two sets of experiments were conducted. The first experiment set focused on step, ramp, and sinusoid tip force control when the robot was not initially actuated. The second set explored the tip force control along the x-, y- and z-axes when the robot was initially actuated to four different configurations using different pressure sequences, i.e., 1) $\mathcal{P}_1 = \mathcal{P}_4 = 0.4$ bar, 2) $\mathcal{P}_1 = \mathcal{P}_4 = 0.6$ bar, 3) $\mathcal{P}_2 = \mathcal{P}_3 = \mathcal{P}_5 = \mathcal{P}_6 = 0.4$ bar, and 4) $\mathcal{P}_2 = \mathcal{P}_3 = \mathcal{P}_5 = \mathcal{P}_6 = 0.6$ bar.

Figures 7(a)-(i) report the tip blocked force control results when the robot is initially not actuated, and Figures 7(j) illustrates the experimental setup for the tip force measurement. The results demonstrate that the force controller is capable of tracking step, ramp and sinusoid forces with a maximum force of 0.45 N, and Figure 7(h) reports that the median force errors for the step and ramp force tracking are below 0.015 N. For the sinusoid force tracking, the overall force errors become larger as the force period decreases from 10 seconds to 2 seconds. For instance, the median errors are 0.041 N, 0.044 N, 0.060 N, 0.081 N 0.152 N when the time periods are 10 s, 8 s, 6 s, 4 s and 2 s, respectively. Similar to Figure 4(b), Figure 7(i) reports that a linear relation between generated tip force and pressure is also observed for a two-segment robot. Using a linear regression, the linear coefficients are 0.54 N/bar, 0.49 N/bar and 0.47 N/bar for the ramp force, sinusoid force (T = 10 s) and sinusoid force (T = 6 s) tests, respectively. Supplementary Video S3 demonstrates this experiment set.

[Figure 7 about here.]

Figure 8 reports results of force control along three axes across four robot configurations (see Figure 8(a)). Figures 8(b)-(e) and Table 3 report constant force control results, with Figures8(f)-(i) showing the corresponding control pressures. In most cases, the average force errors along the x- and y-axes are between 0.01 and 0.03 N with a maximum desired force of 0.4 N. By contrast, the force errors along the z-axis are between 0.01 and 0.05 N with a maximum desired force of 0.6 N. In all tests, the standard deviations of the errors are similar and between 0.01$\sim$0.02 N. Moreover, Figures 8(f)-(i) report that the control pressure of two robot segments is coupled and follows a pattern of $\mathcal{P}_1 = \mathcal{P}_4$, $\mathcal{P}_2 = \mathcal{P}_5$ and $\mathcal{P}_3 = \mathcal{P}_6$ throughout all the tests. This coupling of control pressures demonstrates that both robot segments are controlled in a same manner.

[Figure 8 about here.]

[Table 3 about here.]

Distal-only force control for a two-segment robot by decoupled pressure

This experiment validates the tip force control for a two-segment robot using decoupled pressure across eight robot configurations. Here, only the pressure in the distal segment is controlled to produce desired tip forces, while maintaining chamber pressure invariant in the proximal segment. The initial actuation pressure amplitude was set as 0.5 bar. Desired forces were set as 0.25 N, 0.25 N and 0.4 N along the x-, y- and z-axes, respectively.

[Figure 9 about here.]

The boxplots in Figure 9 indicate that the median force control errors along the x-, y- and z-axes are less than 0.03 N, 0.04 N and 0.06 N, respectively. Figure 9 also reports the corresponding control pressures. The pressure sequences applied during 0$\sim$2 s actuate the robot to different configurations. After 2 s, the pressure in the second robot segment ($\mathcal{P}_4$, $\mathcal{P}_5$ and $\mathcal{P}_6$) varies, as they are calculated by the force controller to achieve desired tip forces. In contrast, the variation of pressure in the first robot segment ($\mathcal{P}_1$, $\mathcal{P}_2$ and $\mathcal{P}_3$, represented by dotted lines) remain relatively constant during the force generation stages. Compared with the pressure sequences in Figures 8(f)-(i), the pressure in Figure 9 indicates that the distal-only force controller effectively decouples the pressure between the two robot segments, allowing only the distal segment to generate tip forces. The pressure amplitudes in Figure 9 reach up to 1.9 bar to generate forces of 0.25 N along the x- and y-axes. Supplementary Video S4 provides a demonstration of this experiment.

Discussions and Conclusion

This paper proposed an on-demand force control method for soft continuum robots based on a compliance model. Our approach is capable of controlling tip forces of soft robots along the x-, y- and z-axes under different robot configurations. The effectiveness of the proposed force controller was validated through experiments with both one- and two-segment robots. Notably, all experiments demonstrated that ramp and step force control errors remained consistently below 0.05 N.

Tables 2 and 3 report that the standard deviation of the force control errors are about $0.008 \sim 0.015$ N, which is in line with measurement resolution of the F/T sensor ($\pm$0.01 N). Additionally, friction between the robot tip and the force sensor may introduce measurement noise. For force control along three axes, the results demonstrate that force errors along the z-axis are usually $0.02 \sim 0.03$ N larger than the errors from the x- and y-axes. This can be explained that the measured force along the z-axis might not be strictly generated by the centre of the robot tip. In our setup, the pressure control system achieves high accuracy, with an error of less than 0.03 bar.[43] The primary source of uncertainty in our model lies in the stiffness parameters, specifically EI_x, EI_y and EA. To address this, we performed experimental parameter identification to obtain the material modulus E, using known design values of L, A, I_x, I_y. Specifically, we identified a pressure-dependent modulus $E(P)$, modelled as a second-order polynomial function, with an R^2 value of 0.984 (see Figure 2(a)). As such, $E(P)$ effectively minimises the model uncertainty arising from robot dimensions, the nonlinear material behaviour and the pressure control error. Throughout this work, the same $E(P)$ was used for all manipulators, with only one-time calibration. While this demonstrates the reusability of $E(P)$, recalibration may become necessary due to material ageing or environmental drift. Prior to experiments, diagnostic tests can be used to assess model accuracy. For instance, by applying a predefined pressure to generate elongation and comparing the measured displacement to the simulated one. If the discrepancy exceeds a set threshold, parameters of $E(P)$ in Figure 2(c) should be updated.

Compared Figure 7 with Figure 3, the maximum controllable tip forces are set as 1.0 N and 0.45 N for one- and two-segment robots, respectively. This is attributed to the fact that the two-segment robot has higher tip compliance and lower tip force generation capability,[39] as evidenced by Figures 4(b) and 7(i), i.e., the force-pressure coefficients are about 1 N/bar and 0.5 N/bar for the one- and two-segment robots, respectively. Interestingly, a linear relationship between the tip blocked force and actuation pressure is also observed in other pneumatic-driven actuators, e.g., fibre-reinforced bending actuator[45] and the PneuNets actuator.[46] The selection of initial pressure values across different experiments is constrained by a maximum allowable pressure of 2 bar, beyond which there is a risk of damaging the robot. For example, for the one-segment robot, we limited the maximum pressure to 1 bar, with peak actuation pressures remaining below 1.7 bar during the force generation. For the two-segment robot, the initial pressure is set around 0.5 bar. As shown in Figure 9(d), the maximum pressure reaches approximately 1.9 bar when the initial pressure is 0.5 bar.

Figures 8 and 9 demonstrate that the second robotic segment requires higher pressure (above

1.9 bar) to generate tip forces when employing the distal-only force control, in contrast to the pressure required (less than 1.5 bar) when using the uniform force control to produce similar forces. This is due to the fact that when executing the distal-only force control, only the second robotic segment contributes to the tip force generation.

In this work, we focused on the (quasi-)static force control where the robot kinematics is based on the static Cosserat rod model, excluding the robot dynamics. As revealed in Figures 3 and 7, the force control errors for one- and two-segment robots become larger when the frequency of desired forces increases. It is worth mentioning that soft robotic systems usually have low bandwidth. e.g., 1 Hz.[47] In our case, the bandwidth of our system is about $0.25 \sim 1$ Hz. Elevating the computation speed of our approach by advancing software and hardware implementation or considering the dynamics of soft robots[13,48,49] could improve the bandwidth of the force controller.

As highlighted in Table 1, our force control approach is exclusively based on the compliance model, without relying on additional force sensing devices. In general, the mean force control errors are less than 5% of the peak desired forces. Although our approach is model-based and open-loop, it is worth mentioning that our achieved control accuracy is comparable to results from existed literature. For instance, about 10% using learning-based approaches,[33] $5 \sim 20\%$ using force sensing-based closed-loop control approaches.[10,15] Compared to closed-loop and learning-based force control, the deployment of feedback loop[22,26] and gathering large training data sets[32,33] are not required in our approach. For example, our approach can be applied on soft robots in visually occluded environments, where exteroceptive measurements are needed to provide deformation information for the force control.[26] As such, our approach is advantageous for applications where size requirements[36] or inherent softness of robots[50] impede sensor implementation. In addition, the identification of the dynamic modulus is conveniently obtained from the elongation-pressure relation. Theoretically, the accuracy of predicted displacement derived by compliance matrix from (5) guarantees under the small deflection assumption,[39] however, satisfying control efficacy can be achieved even large forces are demanded (e.g., see Figure 3).

It is noteworthy that our controller is open-loop, and, as such, cannot adaptively compensate for large environmental uncertainties. For instance, the elastic modulus of soft materials is sensitive to temperature, strain rate, and fatigue. To accommodate these uncertainties, the identified pressure-dependent modulus $E(P)$ in Figure 2(c) can be extended to a multi-dimensional table, incorporating influences of environmental parameters such as temperature and material ageing. Moreover, if force sensing is available, our controller can be integrated as the inner loop within a closed-loop control framework to handle such uncertainties. Another potential limitation of our approach is its applicability to soft robots exhibiting non-uniform deformations, such as ballooning effect, which can significantly alter robots' stiffness properties and reduce the accuracy of the compliance model.

Extending our approach to soft robots with more than two segments requires the consideration of intermediate conditions in Equations S(3) and S(4) reported in the Supplementary Appendix SA1. Specifically, it is essential to ensure force and moment equilibrium, as well as kinematic continuity, at the connections between adjacent segments. Notably, increasing the number of segments introduces kinematic redundancy in the robot. Consequently, additional constraints must be imposed when determining the required actuation pressures. While this added redundancy complicates control, it also enables a wider range of force control strategies. Investigating force control in soft robots with increased segments represents a promising direction for future research.

In this work, we propose a new compliance model-based force control approach intended for soft–rigid interactions, where the environment exhibits significantly higher stiffness than the soft robot. A promising direction for future research is to extend this approach to force control in interactions with compliant environments. In our approach, the interaction force is regulated by controlling desired positions, which complies with the form of stiffness control.[3] As such, future work involves extending our approach to hybrid position and stiffness control[51,52] for real-world

applications, such as soft medical instruments and soft grippers, where the soft manipulators might be required to delicately exert certain amount of forces on organs or objectives.

Author Disclosure Statement

No competing financial interests exist.

Funding Information

This work is supported by the Springboard Award of the Academy of Medical Sciences (grant number: SBF003-1109), the Engineering and Physical Sciences Research Council (grant numbers: EP/R037795/1, EP/S014039/1 and EP/V01062X/1), the Royal Academy of Engineering (grant number: IAPP18-19\264), the UCL Dean's Prize, UCL Mechanical Engineering, and the China Scholarship Council (CSC).

Supplementary Material

Supplementary Appendix SA1
Supplementary Video S1
Supplementary Video S2
Supplementary Video S3
Supplementary Video S4

References

[1] R. F. Shepherd, F. Ilievski, W. Choi, *et al.*, "Multigait soft robot," *Proc Natl Acad Sci*, vol. 108, no. 51, pp. 20400–20403, 2011.

[2] J. Shi, K. Borvorntanajanya, K. Chen, *et al.*, "Design, control and evaluation of a novel soft everting robot for colonoscopy," *IEEE Trans Robot*, vol. 41, pp. 4843–4859, 2025.

[3] C. Ott, R. Mukherjee, and Y. Nakamura, "A hybrid system framework for unified impedance and admittance control," *J Intell Robot Syst*, vol. 78, pp. 359–375, 2015.

[4] A. Stilli, H. A. Wurdemann, and K. Althoefer, "A novel concept for safe, stiffness-controllable robot links," *Soft Robot*, vol. 4, no. 1, pp. 16–22, 2017.

[5] J. Shi, G. Shi, Y. Wu, *et al.*, "A multi-cavity touch interface for a flexible soft laparoscopy device: Design and evaluation," *IEEE Trans. Med. Robot. Bionics*, vol. 6, no. 4, pp. 1309–1321, 2024.

[6] M. Yip, S. Salcudean, K. Goldberg, *et al.*, "Artificial intelligence meets medical robotics," *Science*, vol. 381, no. 6654, pp. 141–146, 2023.

[7] C. Della Santina, C. Duriez, and D. Rus, "Model-based control of soft robots: A survey of the state of the art and open challenges," *IEEE Control Syst Mag*, vol. 43, no. 3, pp. 30–65, 2023.

[8] R. Yasin and N. Simaan, "Joint-level force sensing for indirect hybrid force/position control of continuum robots with friction," *Int J Rob Res*, vol. 40, no. 4-5, pp. 764–781, 2021.

[9] K. Xu and N. Simaan, "An investigation of the intrinsic force sensing capabilities of continuum robots," *IEEE Trans Robot*, vol. 24, no. 3, pp. 576–587, 2008.

[10] A. Bajo and N. Simaan, "Hybrid motion/force control of multi-backbone continuum robots," *Int J Rob Res*, vol. 35, no. 4, pp. 422–434, 2016.

[11] W. Li, X. Huang, L. Yan, *et al.*, "Force sensing and compliance control for a cable-driven redundant manipulator," *IEEE/ASME Trans Mechatron*, pp. 1–12, 2023.

[12] C. B. Black, J. Till, and D. C. Rucker, "Parallel continuum robots: Modeling, analysis, and actuation-based force sensing," *IEEE Trans Robot*, vol. 34, no. 1, pp. 29–47, 2017.

[13] R. K. Katzschmann, C. D. Santina, Y. Toshimitsu, *et al.*, "Dynamic motion control of multi-segment soft robots using piecewise constant curvature matched with an augmented rigid body model," in *IEEE Int Conf Soft Robot*, pp. 454–461, 2019.

[14] C. Della Santina, R. K. Katzschmann, A. Bicchi, *et al.*, "Model-based dynamic feedback control of a planar soft robot: Trajectory tracking and interaction with the environment," *Int J Rob Res*, vol. 39, no. 4, pp. 490–513, 2020.

[15] L. Lindenroth, D. Stoyanov, K. Rhode, *et al.*, "Toward intrinsic force sensing and control in

parallel soft robots," *IEEE/ASME Trans Mechatron*, vol. 28, no. 1, pp. 80–91, 2022.

[16] J. Shi, W. Gaozhang, and H. A. Wurdemann, "Design and characterisation of cross-sectional geometries for soft robotic manipulators with fibre-reinforced chambers," in *IEEE Int. Conf. Soft Robot*, pp. 125–131, 2022.

[17] T. C. Searle, K. Althoefer, L. Seneviratne, and H. Liu, "An optical curvature sensor for flexible manipulators," in *IEEE Int Conf Robot Autom*, pp. 4415–4420, 2013.

[18] H. Zhao, K. O'brien, S. Li, *et al.*, "Optoelectronically innervated soft prosthetic hand via stretchable optical waveguides," *Sci Robot*, vol. 1, no. 1, p. eaai7529, 2016.

[19] X. Cheng, Y. Gong, Y. Liu, *et al.*, "Flexible tactile sensors for dynamic triaxial force measurement based on piezoelectric elastomer," *Smart Mater Struct*, vol. 29, no. 7, p. 075007, 2020.

[20] J.-B. Chossat, Y.-L. Park, R. J. Wood, *et al.*, "A soft strain sensor based on ionic and metal liquids," *IEEE Sens J*, vol. 13, no. 9, pp. 3405–3414, 2013.

[21] S. Chen, H.-Z. Wang, T.-Y. Liu, *et al.*, "Liquid metal smart materials toward soft robotics," *Adv Intell Syst*, p. 2200375, 2023.

[22] C. Tawk, E. Sariyildiz, and G. Alici, "Force control of a 3D printed soft gripper with built-in pneumatic touch sensing chambers," *Soft Robot*, vol. 9, no. 5, pp. 970–980, 2022.

[23] S. E. Navarro, S. Nagels, H. Alagi, *et al.*, "A model-based sensor fusion approach for force and shape estimation in soft robotics," *IEEE Robot Autom Let*, vol. 5, no. 4, pp. 5621–5628, 2020.

[24] P. Abbasi, M. A. Nekoui, M. Zareinejad, *et al.*, "Position and force control of a soft pneumatic actuator," *Soft Robot*, vol. 7, no. 5, pp. 550–563, 2020.

[25] Z. Zhang, J. Dequidt, and C. Duriez, "Vision-based sensing of external forces acting on soft robots using finite element method," *IEEE Robot Autom Let*, vol. 3, no. 3, pp. 1529–1536, 2018.

[26] H. Wang, H. Ni, J. Wang, *et al.*, "Hybrid vision/force control of soft robot based on a deformation model," *IEEE Trans Control Syst Technol*, vol. 29, no. 2, pp. 661–671, 2019.

[27] B. G. Cangan, S. E. Navarro, B. Yang, *et al.*, "Model-based disturbance estimation for a fiber-reinforced soft manipulator using orientation sensing," in *IEEE/RSJ Int Conf Intell Robots Syst*, pp. 9424–9430, 2022.

[28] J. Lai, B. Lu, and H. K. Chu, "Variable-stiffness control of a dual-segment soft robot using depth vision," *IEEE/ASME Trans Mechatron*, vol. 27, no. 2, pp. 1034–1045, 2022.

[29] H. Yang, J. Liu, W. Liu, *et al.*, "Compliant grasping control for a tactile self-sensing soft gripper," *Soft Robot*, vol. 11, no. 2, pp. 230–243, 2024.

[30] C. D. Santina, R. L. Truby, and D. Rus, "Data–driven disturbance observers for estimating external forces on soft robots," *IEEE Robot Autom Let*, vol. 5, no. 4, pp. 5717–5724, 2020.

[31] X. Chen, J. Shi, H. Wurdemann, *et al.*, "Vision-based tip force estimation on a soft continuum robot," in *IEEE Int Conf Robot Autom*, pp. 7621–7627, 2024.

[32] S. Joshi and J. Paik, "Sensorless force and displacement estimation in soft actuators," *Soft Matter*, vol. 19, no. 14, pp. 2554–2563, 2023.

[33] T. George Thuruthel, P. Gardner, and F. Iida, "Closing the control loop with time-variant embedded soft sensors and recurrent neural networks," *Soft Robot*, vol. 9, no. 6, pp. 1167–1176, 2022.

[34] S. Francesco, H. Josie, R. Daniela, *et al.*, "Prescribing Cartesian stiffness of soft robots by co-optimization of shape and segment-level stiffness," *Soft Robot*, vol. 10, no. 4, pp. 701–712, 2023.

[35] N. Kumar, J. Wirekoh, S. Saba, *et al.*, "Soft miniaturized actuation and sensing units for dynamic force control of cardiac ablation catheters," *Soft Robot*, vol. 8, no. 1, pp. 59–70, 2021.

[36] J. Burgner-Kahrs, D. C. Rucker, and H. Choset, "Continuum robots for medical applications: A survey," *IEEE Trans Robot*, vol. 31, no. 6, pp. 1261–1280, 2015.

[37] J. Shi, H. Jin, S.-A. Abad, *et al.*, "A static modelling and evaluation framework for soft continuum robots with reinforced chambers," *IEEE Trans Robot*, vol. 41, pp. 6419–6439, 2025.

[38] D. C. Rucker and R. J. Webster, "Computing jacobians and compliance matrices for externally loaded continuum robots," in *IEEE Int Conf Robot Autom*, pp. 945–950, 2011.

[39] J. Shi, A. Shariati, S.-A. Abad, *et al.*, "Stiffness modelling and analysis of soft fluidic-driven robots using Lie theory," *Int J Rob Res*, vol. 43, no. 3, pp. 354–384, 2024.

[40] J. Shi, S. Abad Guaman, J. Dai, *et al.*, "Position and orientation control for hyperelastic multi-segment continuum robots," *IEEE/ASME Trans Mechatron*, vol. 29, no. 2, pp. 995–1006, 2024.

[41] J. Till, V. Aloi, and C. Rucker, "Real-time dynamics of soft and continuum robots based on cosserat rod models," *Int J Rob Res*, vol. 38, no. 6, pp. 723–746, 2019.

[42] C. B. Teeple, T. N. Koutros, M. A. Graule, *et al.*, "Multi-segment soft robotic fingers enable robust precision grasping," *Int J Rob Res*, vol. 39, no. 14, pp. 1647–1667, 2020.

[43] J. Shi, W. Gaozhang, H. Jin, *et al.*, "Characterisation and control platform for pneumatically driven soft robots: Design and applications," in *IEEE Int. Conf. Soft Robot*, pp. 1–8, 2023.

[44] E. Porte, S. Eristoff, A. Agrawala, *et al.*, "Characterization of temperature and humidity dependence in soft elastomer behavior," *Soft Robot*, vol. 11, no. 1, pp. 118–130, 2024.

[45] P. Polygerinos, Z. Wang, J. T. Overvelde, *et al.*, "Modeling of soft fiber-reinforced bending actuators," *IEEE Trans Robot*, vol. 31, no. 3, pp. 778–789, 2015.

[46] Sachin, Z. Wang, and S. Hirai, "Analytical modeling of a soft pneu-net actuator subjected to planar tip contact," *IEEE Trans Robot*, vol. 38, no. 5, pp. 2720–2733, 2022.

[47] G. Fang, M. C. Chow, J. D. Ho, *et al.*, "Soft robotic manipulator for intraoperative MRI-guided transoral laser microsurgery," *Sci Robot*, vol. 6, no. 57, p. eabg5575, 2021.

[48] F. Renda, F. Boyer, J. Dias, *et al.*, "Discrete cosserat approach for multisection soft manipulator dynamics," *IEEE Trans Robot*, vol. 34, no. 6, pp. 1518–1533, 2018.

[49] L. Xun, G. Zheng, and A. Kruszewski, "Cosserat-rod based dynamic modeling of soft slender robot interacting with environment," *IEEE Trans Robot*, vol. 40, pp. 2811–2830, 2024.

[50] J. Y. Loo, Z. Y. Ding, V. M. Baskaran, *et al.*, "Robust multimodal indirect sensing for soft robots via neural network-aided filter-based estimation," *Soft Robot*, vol. 9, no. 3, pp. 591–612, 2022.

[51] M. Mahvash and P. E. Dupont, "Stiffness control of surgical continuum manipulators," *IEEE Trans Robot*, vol. 27, no. 2, pp. 334–345, 2011.

[52] J. Shi, S.-A. Abad, G. Shi, *et al.*, "Model-based static compliance analysis and control for pneumatic-driven soft robots," *IEEE/ASME Trans Mechatron*, pp. 1–12, 2025.

[53] Y. Li, Y. Chen, and Y. Li, "Pre-charged pneumatic soft gripper with closed-loop control," *IEEE Robot Autom Let*, vol. 4, no. 2, pp. 1402–1408, 2019.

List of Figures

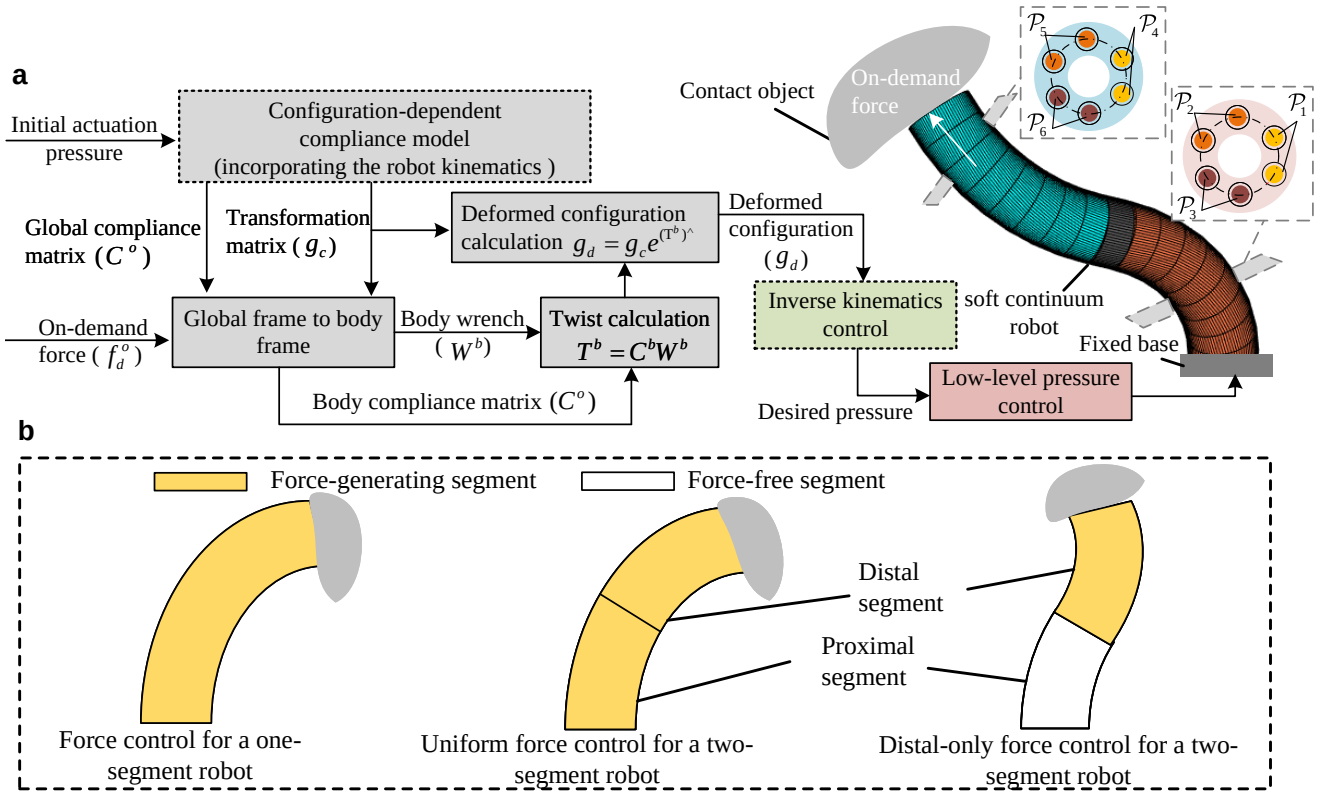

Figure 1. (**a**) Model-based, on-demand force control architecture based on the compliance modelling and solving inverse kinematics problems. (**b**) Various force control modes, including force control for a one-segment robot, uniform force control and distal-only force control for a two-segment robot.

a

Symbols	Description	Dimensions
L_1	Chamber length of the first segment	42.0 [mm]
L_2	Chamber length of the second segment	42.0 [mm]
L_k	Length of the robot connection part	6.0 [mm]
R_{ro}	Radius of the segment	12.5 [mm]
R_{ri}	Radius of the central channel	4.5 [mm]
R_c	Radius of the actuation chamber	2.25 [mm]
A	Cross-sectional area	331.83 [mm^2]
I_x	Second moment of area around the x-axis	1.87×10^4 [mm^4]
I_y	Second moment of area around the y-axis	1.87×10^4 [mm^4]
J_z	Second moment of area around the z-axis	3.75×10^4 [mm^4]
β_1	Coefficient for the dynamic modulus	33640 [1/Pa]
β_2	Coefficient for the dynamic modulus	-104200
β_3	Coefficient for the dynamic modulus	136500 [Pa]

Cross section

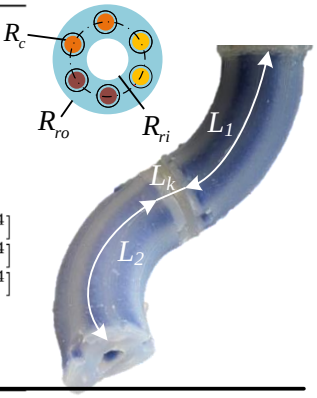

b

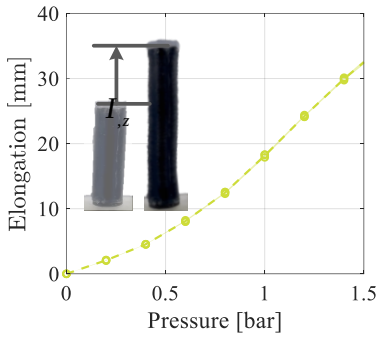

c

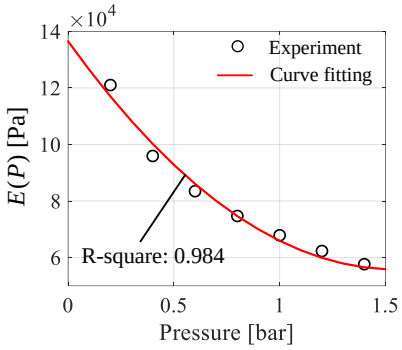

Figure 2. Results of the parameter identification. (**a**) The geometrical parameters of the robot. (**b**) The experimental elongation versus pressure curve. (**c**) The pressure-dependent modulus $E(P)$ with respect to the averaged chamber pressure.

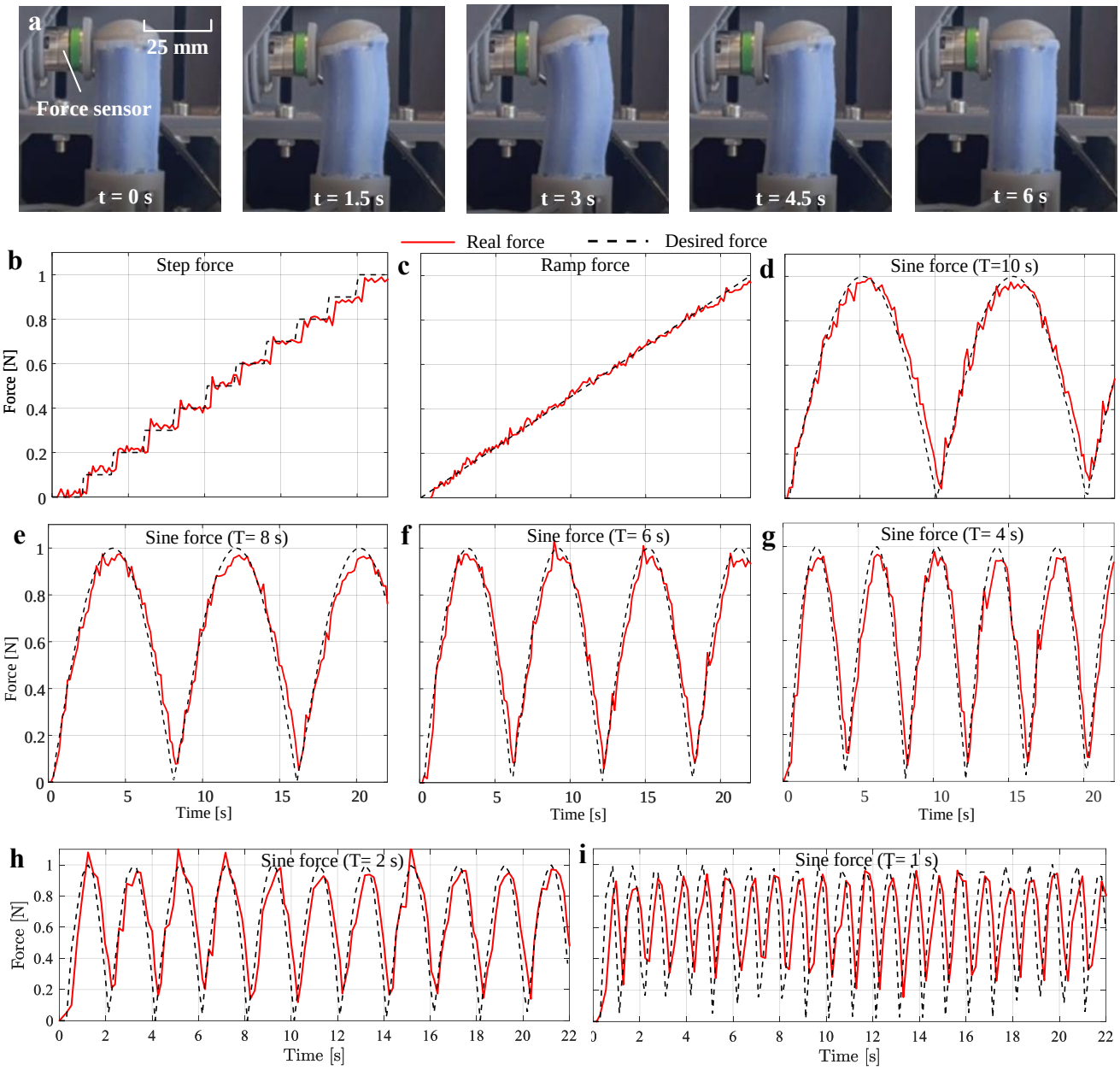

Figure 3. Results of the tip blocked force control for a one-segment robot: (**a**) snapshots for the time-varying tip force control and the force period is 6 s. (**b**) Step force control. (**c**) Ramp force control. Sinusoid force control when the force period is (**d**) 10 s, (**e**) 8 s, (**f**) 6 s, (**g**) 4 s, (**h**) 2 s, and (**i**) 1 s.

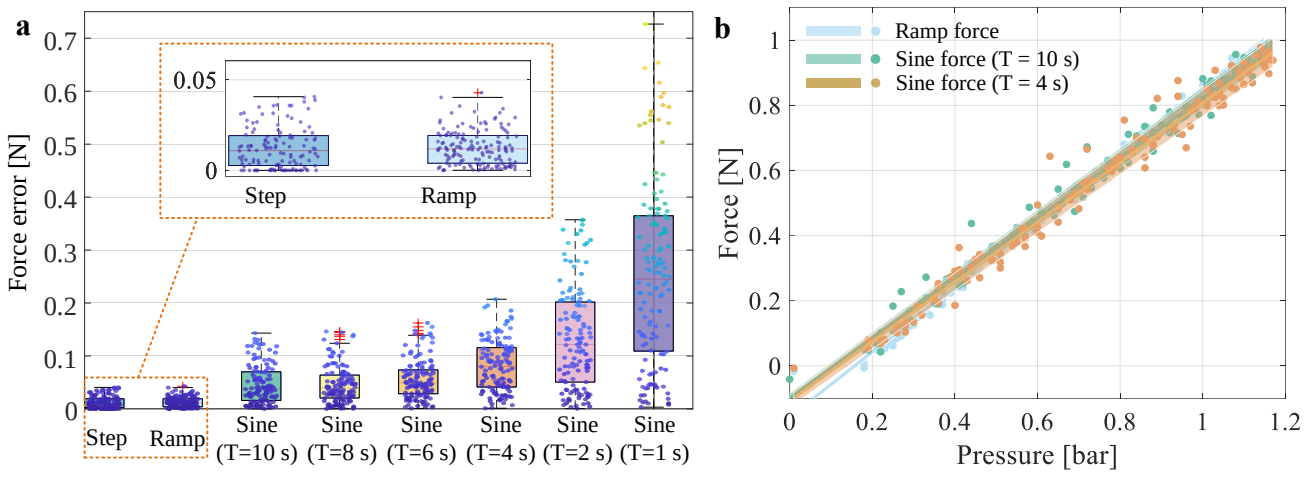

Figure 4. Results of the tip blocked force control of a one-segment robot. (**a**) Summary of the tip blocked force control errors using boxplots. The colour depth of the scattered points indicates the level of errors, e.g., the error increases when the colour varies from blue to orange. (**b**) Relation between the control pressure and the generated tip force using a linear regression.

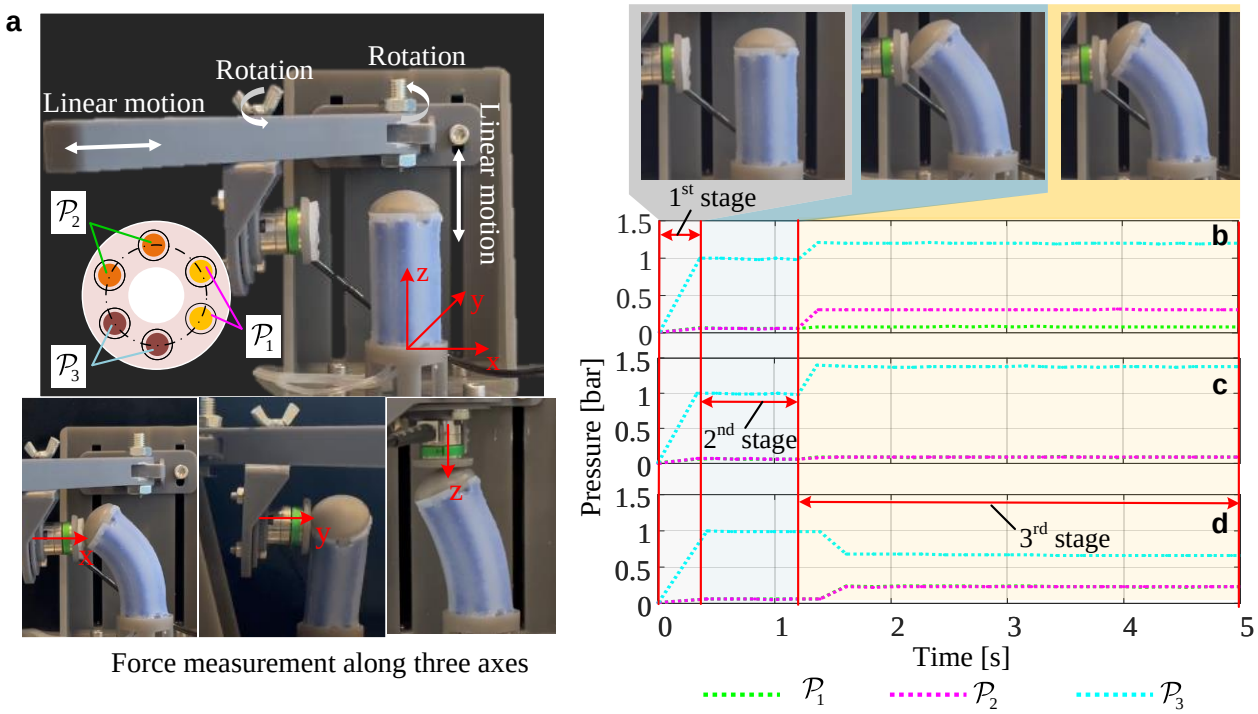

Figure 5. Results of the force control along three axes. Force measurement setup is shown in (**a**). The three-stage pressure sequences defined in Figure 1(a)) for generating forces along x-, y- and z-axes are reported in (**b**), (**c**), and (**d**), respectively. In the first stage, the robot is actuated to a certain configuration. In the second stage, the actuation keeps for 1.0 s, e.g., $\mathcal{P}_3 = 1.0$ bar in this figure. In the third stage, the force controller calculates the actuation pressure to generate a desired tip force.

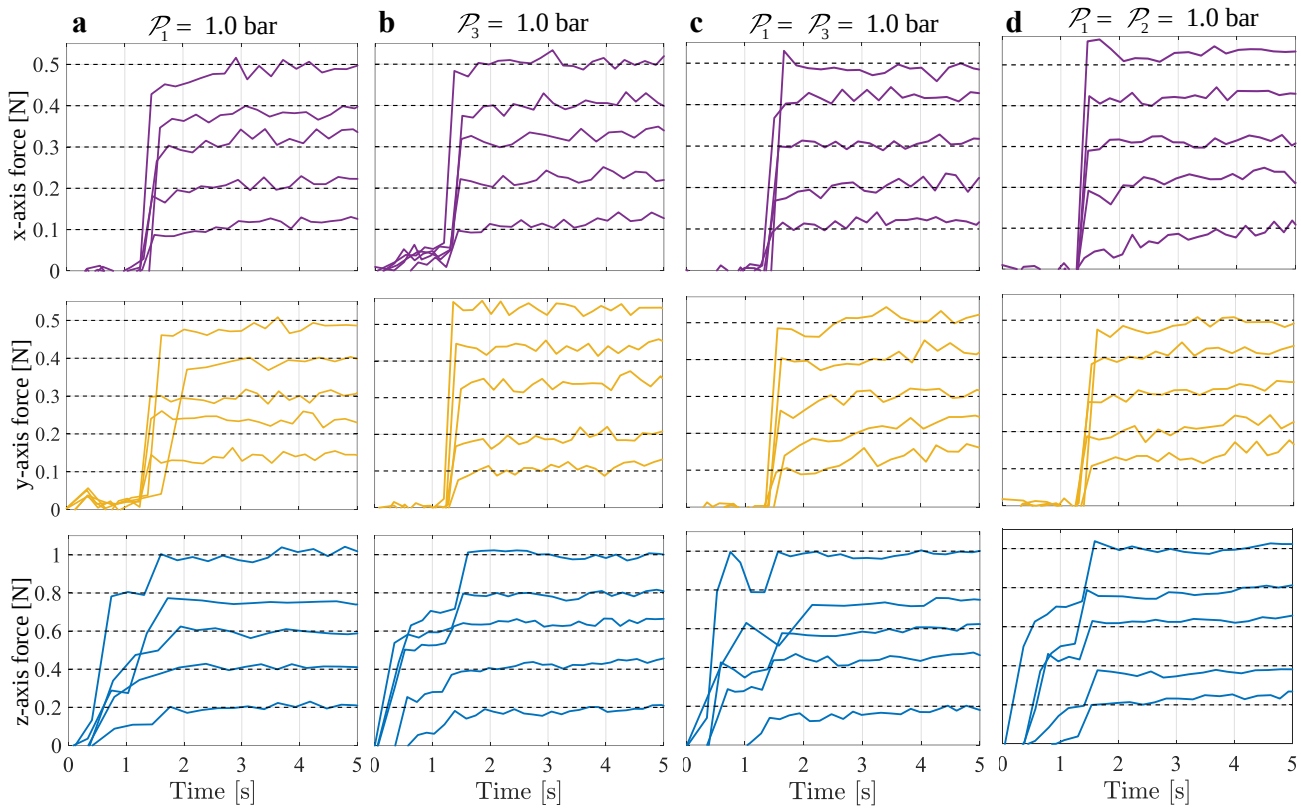

Figure 6. Results of the force control along three axes under four different configurations when (**a**) $\mathcal{P}_1$ = 1.0 bar, (**b**) $\mathcal{P}_3$ = 1.0 bar, (**c**) $\mathcal{P}_1 = \mathcal{P}_3$ = 1.0 bar, and (**d**) $\mathcal{P}_1 = \mathcal{P}_2 = 1.0$ bar. Forces along the x-, y- and z-axes are reported from the top to the bottom.

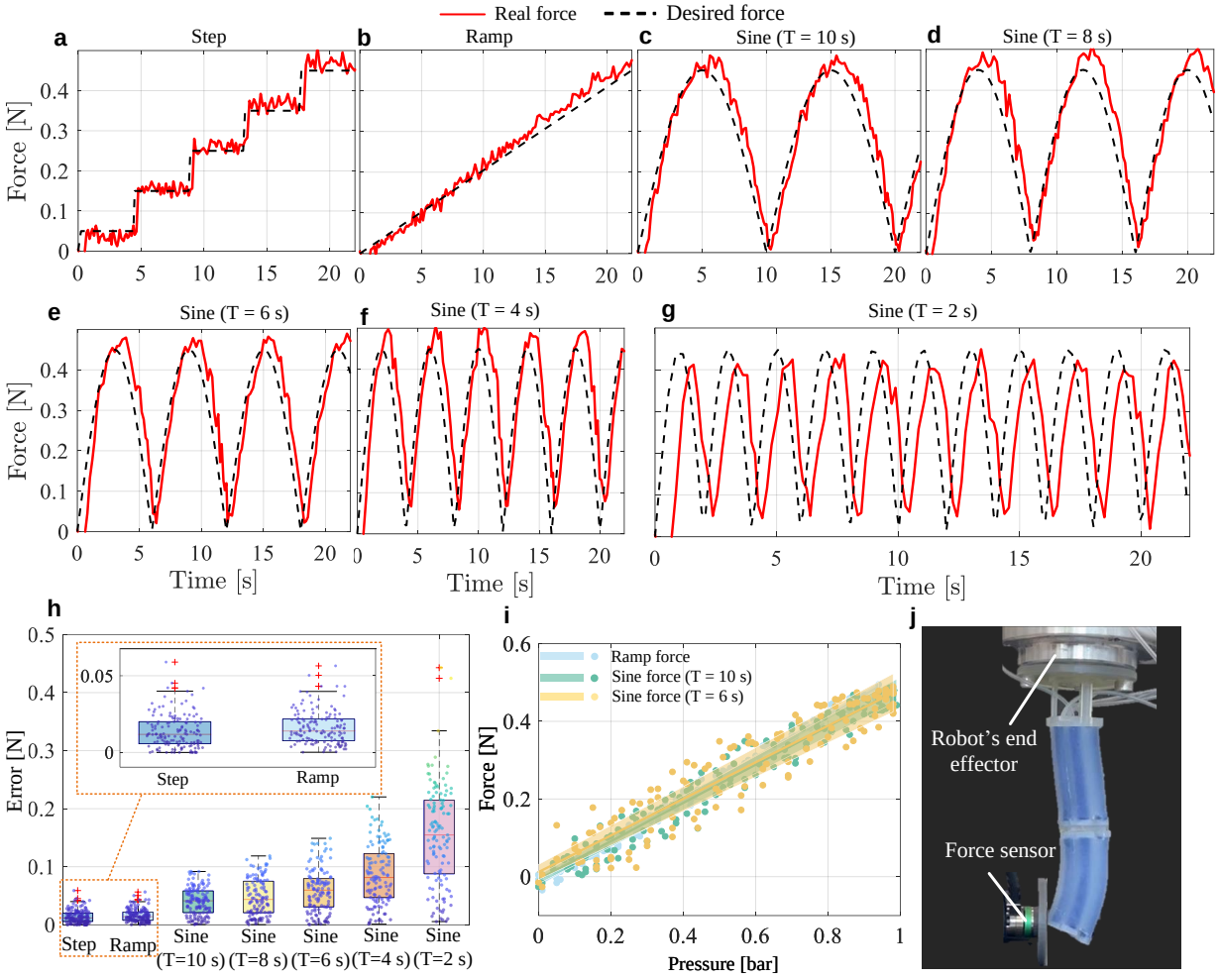

Figure 7. Results of the tip blocked force control for a two-segment robot by the uniform force control when the robot is initially not actuated. (**a**) Step force control. (**b**) Ramp force control. Sinusoid force control when the force period is (**c**) 10 s, (**d**) 8 s, (**e**) 6 s, (**f**) 4 s and (**g**) 2 s. (**h**) The summarised force control errors. (**i**) The linear pressure-force relation. (**j**) Experimental setup for the tip force measurement.

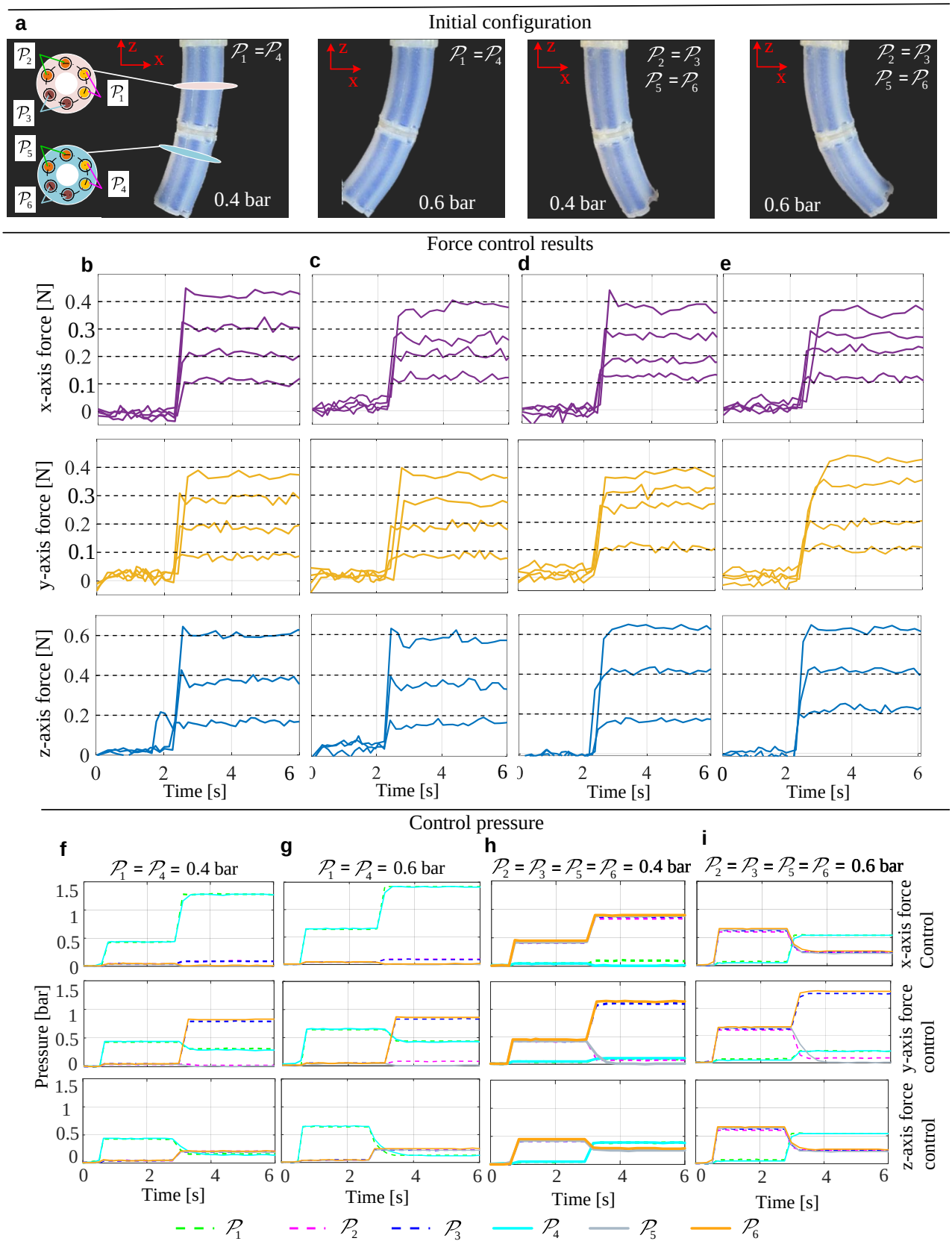

Figure 8. Results of the tip force control along three axes for a two-segment robot by coupled pressure when the robot is initially actuated to four configurations. (**a**) Four robot configurations. The corresponding force control results are reported in (**b**)-(**e**). (**f**)-(**i**) report the control pressure sequences for control when controlling forces of 0.4 N, 0.4 N and 0.6 N along the x-, y-, and z-axes.

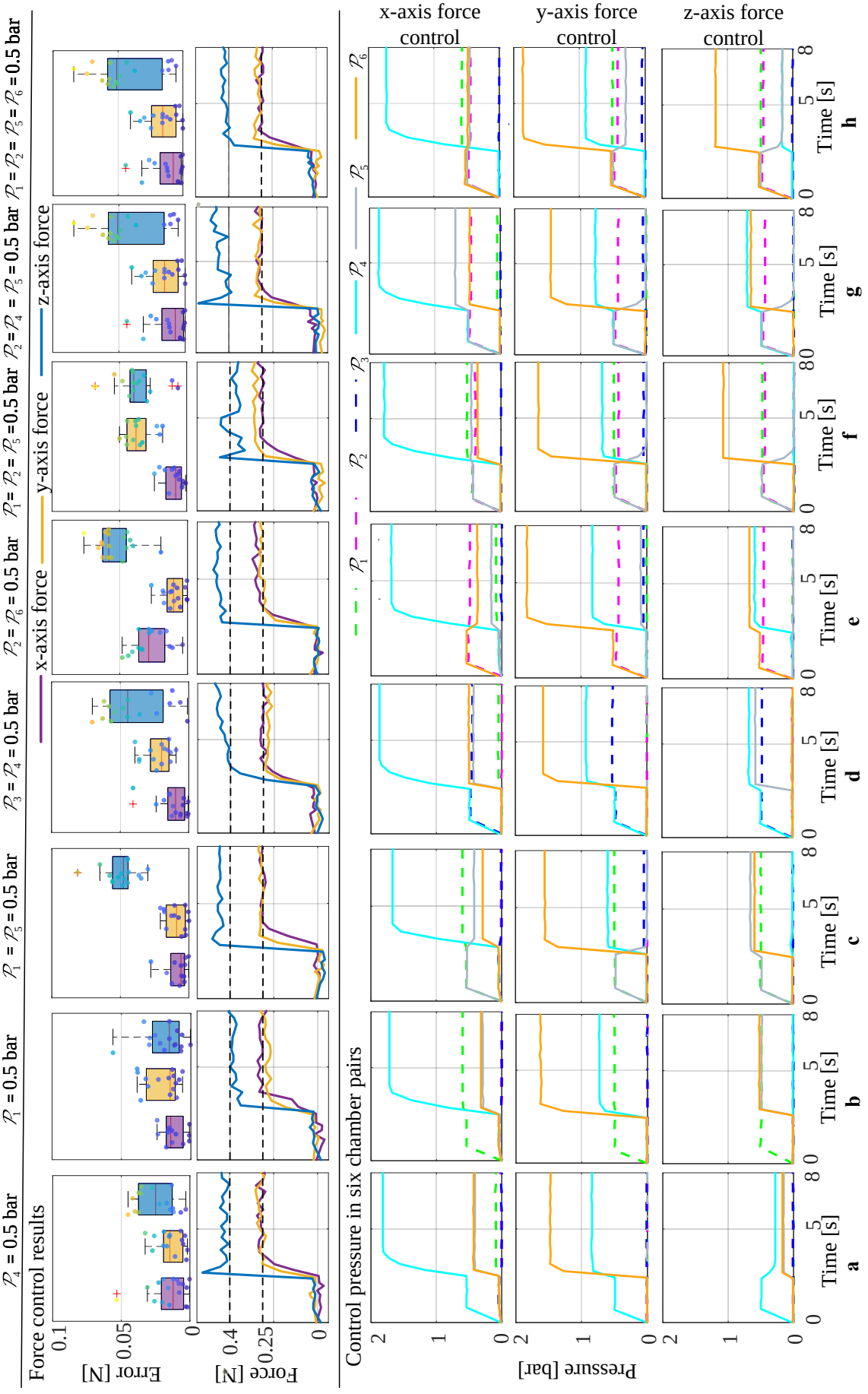

Figure 9. Results of the uniform force control along three axes for a two-segment robot by decoupled pressure. Results when (**a**) $\mathcal{P}_4 = 0.5$ bar, (**b**) $\mathcal{P}_1 = 0.5$ bar, (**c**) $\mathcal{P}_1 = \mathcal{P}_5 = 0.5$ bar, (**d**) $\mathcal{P}_3 = \mathcal{P}_4 = 0.5$ bar, (**e**) $\mathcal{P}_2 = \mathcal{P}_6 = 0.5$ bar, (**f**) $\mathcal{P}_1 = \mathcal{P}_2 = \mathcal{P}_5 = 0.5$ bar, (**g**) $\mathcal{P}_2 = \mathcal{P}_4 = \mathcal{P}_5 = 0.5$ bar, and (**h**) $\mathcal{P}_1 = \mathcal{P}_2 = \mathcal{P}_5 = \mathcal{P}_6 = 0.5$ bar. The force errors are box-plotted. Please note that two robotic segments initially bend in different planes in (c)-(g).

List of Tables

Table 1. Comparison of force control techniques for soft robotic systems

References	*Force sensing device*	*Force sensing principle*	*Force control principle*	*Control error*	*Multi-axis force control*
Lindenroth et al.[15]	Required	Fluidic pressure & volume	Closed-loop PID control	$\approx 10 \sim 20\%$	Yes
Tawk et al.[22]	Required	Fluidic pressure	Closed-loop PID control	–	No
Wang et al.[26]	Required	Vision	Closed-loop PD control	–	No
Yang et al.[29]	Required	Optical tactile sensing	Learning-based, closed-loop control	$< 2.17\%$	No
Thuruthel et al.[33]	Required	Strain sensors	Learning-based, closed-loop control	$\approx 10\%$	No
Li et al.[53]	Required	Flexible force sensor	Closed loop control	$6 \sim 13\%$	No
Our work	Not required	Not required	Compliance model-based, open-loop control	$< 5\%$	Yes

* The control error is defined as the ratio of the force error to the desired force value.

Table 2. Results of the force control along three axes: Mean and standard deviation of steady-state force control errors

Configuration	*Force axis*	*Desired forces along the x- or y-axes*				
		0.1 [N]	*0.2 [N]*	*0.3 [N]*	*0.4 [N]*	*0.5 [N]*
$\mathcal{P}_1$ = 1.0 bar	x-axis	0.0164 ± 0.0093	0.0137 ± 0.0100	0.0231 ± 0.0155	0.0188 ± 0.0119	0.0186 ± 0.0125
	y-axis	0.0422 ± 0.0123	0.0364 ± 0.0111	0.0111 ± 0.0067	0.0108 ± 0.0099	0.0200 ± 0.0096
$\mathcal{P}_3$ = 1.0 bar	x-axis	0.0231 ± 0.0149	0.0284 ± 0.0135	0.0311 ± 0.0156	0.0112 ± 0.0112	0.0109 ± 0.0079
	y-axis	0.0139 ± 0.0091	0.0165 ± 0.0106	0.0369 ± 0.0153	0.0393 ± 0.0132	0.0433 ± 0.0119
$\mathcal{P}_1 = \mathcal{P}_3$ = 1.0 bar	x-axis	0.0282 ± 0.0152	0.0248 ± 0.0158	0.0241 ± 0.0137	0.0290 ± 0.0145	0.0114 ± 0.0091
	y-axis	0.0588 ± 0.0225	0.0437 ± 0.0198	0.0255 ± 0.0152	0.0363 ± 0.0202	0.0292 ± 0.0179
$\mathcal{P}_1 = \mathcal{P}_2$ = 1.0 bar	x-axis	0.0221 ± 0.0126	0.0398 ± 0.0184	0.0305 ± 0.0174	0.0368 ± 0.0158	0.0158 ± 0.0369
	y-axis	0.0460 ± 0.0204	0.0223 ± 0.0133	0.0194 ± 0.0129	0.0209 ± 0.0132	0.0133 ± 0.0093
Configuration	*Force axis*	*Desired forces along the z-axis*				
		0.2 [N]	*0.4 [N]*	*0.6 [N]*	*0.8 [N]*	*1.0 [N]*
$\mathcal{P}_1$ = 1.0 bar	z-axis	0.0183 ± 0.0137	0.0242 ± 0.0121	0.0124 ± 0.0091	0.0484 ± 0.0100	0.0336 ± 0.0217
$\mathcal{P}_3$ = 1.0 bar	z-axis	0.0170 ± 0.0121	0.0376 ± 0.0209	0.0520 ± 0.0167	0.0127 ± 0.0111	0.0111 ± 0.0132
$\mathcal{P}_1 = \mathcal{P}_3$ = 1.0 bar	z-axis	0.0295 ± 0.0209	0.0539 ± 0.0207	0.0191 ± 0.0113	0.0611 ± 0.0176	0.0188 ± 0.0138
$\mathcal{P}_1 = \mathcal{P}_2$ = 1.0 bar	z-axis	0.0445 ± 0.0224	0.0304 ± 0.0143	0.0396 ± 0.0149	0.0261 ± 0.0183	0.0176 ± 0.0114

* The reported results have the form of $a \pm b$, where a denotes the mean error and b denotes the standard deviation of the error.

Table 3. Results of the force control along three axes for a two-segment robot by coupled pressure: Mean and standard deviation of steady-state force control errors

Configuration	*Force axis*	*Desired forces along the x- or y-axes*			
		0.1 [N]	*0.2 [N]*	*0.3 [N]*	*0.4 [N]*
$\mathcal{P}_1$ = 0.4 bar	x-axis	0.0132 ± 0.0082	0.0109 ± 0.0085	0.0108 ± 0.0114	0.0235 ± 0.0114
	y-axis	0.0156 ± 0.0086	0.0162 ± 0.0097	0.0127 ± 0.0109	0.0305 ± 0.0091
$\mathcal{P}_1$ = 0.6 bar	x-axis	0.0227 ± 0.0095	0.0123 ± 0.0107	0.0377 ± 0.0152	0.0192 ± 0.0159
	y-axis	0.0178 ± 0.0085	0.0141 ± 0.0091	0.0273 ± 0.0101	0.0317 ± 0.0086
$\mathcal{P}_2 = \mathcal{P}_3 = \mathcal{P}_5$	x-axis	0.0228 ± 0.0081	0.0190 ± 0.0088	0.0278 ± 0.0110	0.0237 ± 0.0134
$= \mathcal{P}_6 = 0.4$ bar	y-axis	0.0123 ± 0.0077	0.0624 ± 0.0087	0.0227 ± 0.0099	0.0190 ± 0.0129
$\mathcal{P}_2 = \mathcal{P}_3 = \mathcal{P}_5$	x-axis	0.0170 ± 0.0087	0.0196 ± 0.0105	0.0273 ± 0.0087	0.0381 ± 0.0146
$= \mathcal{P}_6 = 0.4$ bar	y-axis	0.0089 ± 0.0047	0.0106 ± 0.0092	0.0388 ± 0.0108	0.0271 ± 0.0087

Configuration	*Force axis*	*Desired forces along the z-axis*		
		0.2 [N]	*0.4 [N]*	*0.6 [N]*
$\mathcal{P}_1$ = 0.4 bar	z-axis	0.0344 ± 0.0125	0.0271 ± 0.0153	0.0094 ± 0.0082
$\mathcal{P}_1$ = 0.6 bar	z-axis	0.0375 ± 0.0132	0.0487 ± 0.0172	0.0153 ± 0.0094
$\mathcal{P}_2 = \mathcal{P}_3 = \mathcal{P}_5$ $= \mathcal{P}_6 = 0.4$ bar	z-axis	0.0315 ± 0.0090	0.0180 ± 0.0109	0.0359 ± 0.0106
$\mathcal{P}_2 = \mathcal{P}_3 = \mathcal{P}_5$ $= \mathcal{P}_6 = 0.6$ bar	z-axis	0.0375 ± 0.0132	0.0487 ± 0.0172	0.0294 ± 0.0131

* The reported results have the form of $a \pm b$, where a denotes the mean error and b denotes the standard deviation of the error.

Supplementary Material for Compliance Model-based Contact Force Control for Soft Continuum Robots

Jialei Shi*¶, Sara-Adela Abad*†, Jian S Dai‡§, and Helge Wurdemann*

APPENDIX 1. SUPPLEMENTARY DETAILS FOR THE ANALYTICAL MODEL

Building on the compliance modelling framework proposed in [1], analytical forms for $l_P(s)$, $f_P(s)$, $F_P(t^-)$, $m_P(t^-)$, and b_c are summarised in this documents.

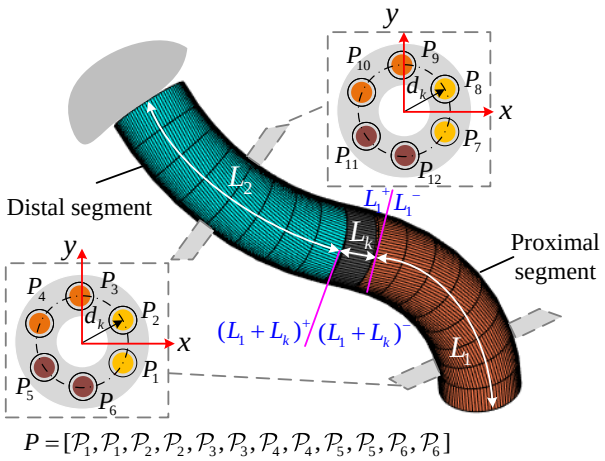

Fig. S1. illustration of a two-segment robot. Each segment has three chamber pairs denoted using a same colour.

$f_P(s)$ and $l_P(s)$ are the distributed force and moment resulting from pressurisation and equal

$$f_P(s) = \sum_{k=h}^{5+h} [P_k A_c R_s(s) e_3], \;\; m_P(s) = \sum_{k=h}^{5+h} P_k A_c R(s)[(v(s) + \hat{u}(s) d_k) \times e_3 + \hat{d}_k \hat{u}(s) e_3)], \tag{S1}$$

where P_k is the kth entry of the pressure vector P, A_c is the chamber area, $\hat{d}_k$ is the skew position vector of the kth chamber, $e_3 = [0, 0, 1]^T$. Please note that $h \in [1, 6]$ and $h \in [7, 12]$ for the proximal and the distal robotic segments, respectively. Details are illustrated in Fig. S1.

$F_P(t^-)$ and $m_P(t^-)$ are the total pressurisation force and moment at the robot's tip in the body framework, which yields

$$F_P(t^-) = \sum_{k=h}^{5+h} A_c P_k e_3, \;\; m_P(t^-) = \sum_{k=h}^{5+h} d_k \times A_c P_k e_3. \tag{S2}$$

Here, $t = L_1$ or $t = L_2$ for a one-segment robot; $t = L_1 + L_k + L_2$ for a two-segment robot. Superscripts $^-$ and $^+$ denote the left and right limits (see Fig. S1), respectively.

b_c includes intermediate boundary conditions for a two-segment robot. Assuming a rigid connection between two robot segments without applied forces and/or moments at the end of L_1, the force and moment balances in intermediate boundary conditions are

$$\begin{aligned}
&n(L_1^-) = R(L_1^-) F_P(L_1^-) + n(L_1^+), \\
&m(L_1^-) = R(L_1^-) m_P(L_1^-) + m(L_1^+), \\
&n((L_1+L_k)^-) = n((L_1+L_k)^+) - R((L_1+L_k)^+) F_P((L_1+L_k)^+), \\
&m((L_1+L_k)^-) = m((L_1+L_k)^+) - R((L_1+L_k)^+) m_P((L_1+L_k)^+).
\end{aligned} \tag{S3}$$

¶Hamlyn Centre for Robotic Surgery, Department of Mechanical Engineering, Imperial College London, UK.
*Department of Mechanical Engineering, University College London, UK.
†Universidad Nacional de Loja, Loja, Ecuador.
§Institute for Robotics, Southern University of Science and Technology, Shenzhen, China.
‡Centre for Robotics Research, Department of Engineering, King's College London, UK.

$F_P(L_1^-)$, $m_P(L_1^-)$, $F_P((L_1+L_k)^+)$ and $m_P((L_1+L_k)^+)$ are derived according to (S2). b_c also includes the kinematic continuity across the connection part between two robot segments, yielding

$$\begin{aligned} &p(L_1^-) = p(L_1^+),\ R(L_1^-) = R(L_1^+), \\ &p((L_1+L_k)^-) = p((L_1+L_k)^+),\ R((L_1+L_k)^-) = R((L_1+L_k)^+). \end{aligned} \tag{S4}$$

Equation (S4) denotes that the kinematic continuity needs to consider both the position and orientation at connection parts.

REFERENCES

[1] J. Shi, A. Shariati, S.-A. Abad *et al.*, "Stiffness modelling and analysis of soft fluidic-driven robots using Lie theory," *Int J Rob Res*, vol. 43, no. 3, pp. 354–384, 2024.